Journal of Alloys and Compounds 826 (2020) 154194

Contents lists available at ScienceDirect

Journal of Alloys and Compounds

journal homepage: http://www.elsevier.com/locate/jalcom

Unconventional magnetism of non-uniform distribution of Co in TiO_2 nanoparticles

Anatoly Ye Yermakov [a, b], Danil W. Boukhvalov [b, c], Alexey S. Volegov [b], Mikhail A. Uimin [a, b], Galina S. Zakharova [d], Alexander V. Korolev [a], Eugene V. Rosenfeld [a], Vitaly V. Mesilov [a], Artem S. Minin [a, b], Vadim R. Galakhov [a, b, e, *], Leonid S. Molochnikov [f], Andrei F. Gubkin [a], Aidar M. Murzakaev [g], Sergey F. Konev [b]

[a] M. N. Mikheev Institute of Metal Physics, Ural Branch of the Russian Academy of Sciences, Yekaterinburg, 620108, Russia
[b] Ural Federal University, Yekaterinburg, 620002, Russia
[c] College of Science, Institute of Materials Physics and Chemistry, Nanjing Forestry University, Nanjing, 210037, PR China
[d] Institute of Solid State Chemistry, Ural Branch of the Russian Academy of Sciences, Yekaterinburg, 620990, Russia
[e] Ural State Mining University, Yekaterinburg, 620144, Russia
[f] Ural State Forest Engineering University, Yekaterinburg, 620100, Russia
[g] Institute of Electrophysics, Ural Branch of the Russian Academy of Sciences, Yekaterinburg, 620016, Russia

ARTICLE INFO

Article history:
Received 19 December 2019
Received in revised form
31 January 2020
Accepted 4 February 2020
Available online 8 February 2020

ABSTRACT

High-resolution transmission electron microscopy (HRTEM), X-ray diffraction (XRD) analysis, electron paramagnetic resonance (EPR), X-ray absorption spectroscopy (XAS), magnetic methods, and density-functional theory (DFT) calculations were applied for the investigations of Co-doped anatase TiO_2 nanoparticles (~ 20 nm). It was found that high-spin Co^{2+} ions prefer to occupy the interstitial positions in the TiO_2 lattice which are the most energetically favourable in compare to the substitutional those. A quantum mechanical model which operates mainly on two types of $Co^{2+} - Co^{2+}$ dimers with different negative exchange interactions and the non-interacting paramagnetic Co^{2+} ions provides a satisfactorily description of magnetic properties for the TiO_2:Co system.

1. Introduction

There are many examples in the literature of the creation of the ferromagnetic contribution (FM) at room temperature (RT) based on the diluted semiconductors TiO_2, ZnO, SnO_2 without or doped with 3*d* metals [1,2]. It was discussed using various explanations, including polaron states, itinerant magnetism, Ruderman – Kittel – Kasuya – Yosida (RKKY) approach, the influence of vacancies, etc. [3–8]. However, these conclusions are mostly presumptive and have not reliable proofs. In the most of the works, an influence of magnetic impurities and the formation of magnetic segregations of the nanocrystalline materials, for instance, in the particle's surface, were not taken into account [9–12]. These factors may be the main reason for the appearance of a spontaneous magnetic moment in these systems. In this work we study the ground magnetic and electronic states of nanocrystalline Co doped TiO_2 nanopowders with dopant concentrations less than 5 at.% of Co. These nanopowders have the anatase structure in the as-prepared state without any heat treatment.

Note if the content of 3*d* dopants is a few percent, then it is most likely that the exchange interaction will be effective only between the nearest carriers of the magnetic moments [13–19]. Previously, magnetic properties of TiO_2:Fe were successfully described using a dimer model that takes into account two types of dimers with the negative exchange interaction and the paramagnetic contribution [20]. The present study was undertaken to test the applicability of a similar model to describe the magnetic properties of cobalt doped TiO_2.

High resolution transmission electron microscopy (HRTEM), X-

* Corresponding author. M. N. Mikheev Institute of Metal Physics, Ural Branch of the Russian Academy of Sciences, Yekaterinburg, 620108, Russia.
E-mail addresses: yermakov@imp.uran.ru (A.Y. Yermakov), 2018170@njfu.edu.cn (D.W. Boukhvalov), alexey.volegov@urfu.ru (A.S. Volegov), uimin@imp.uran.ru (M.A. Uimin), Volkov@ihim.uran.ru (G.S. Zakharova), korolyov@imp.uran.ru (A.V. Korolev), rosenfeld@imp.uran.ru (E.V. Rosenfeld), mesilov@imp.uran.ru (V.V. Mesilov), minin_a@imp.uran.ru (A.S. Minin), galakhov@ifmlrs.uran.ru (V.R. Galakhov), agubkin@imp.uran.ru (A.F. Gubkin), aidar@iep.uran.ru (A.M. Murzakaev), ksf50@bk.ru (S.F. Konev).

https://doi.org/10.1016/j.jallcom.2020.154194
0925-8388/

ray diffraction (XRD) analysis, electron paramagnetic resonance (EPR), X-ray absorption spectroscopy (XAS), and magnetic methods were used to investigate the structure and the valency states of cations in the mentioned system. The DFT calculations were applied to determine the Co spin state and the character of the band structure. Moreover, the DFT approach can clarify the type of Co solid solutions in the TiO_2 matrix and allows to establish the most favourable configurations for Co^{2+}- Co^{2+} complexes in the system.

2. Experimental

The conventional hydrothermal method was used for the synthesis of the TiO_2:Co nanopowders [21]. The following start compounds were used to produce the nanocrystalline powders: a 15% solution of titanium chloride (III, Merck) in a 10% solution of HCl, cobalt (II) chloride hexahydrate $CoClCoCl_2 \times 6H_2O$, and a 25% aqueous solution of ammonia grade chemically pure. The synthesis of the nanocrystalline titanium-dioxide powders doped with cobalt ions was carried out as follows: the $CoClCoCl_2 6H_2O$ powder was dissolved in $TiCl_3$ in a given molar ratio, then NH_4OH was added dropwise under constant stirring until $pH = 9.2$ was reached. The reactive mixture was placed in an autoclave, kept at 160°C for 24 h, and then cooled down to room temperature under atmospheric conditions. The resulting product was filtered, washed with water (until water reaches neutral *p*H). and dried in air at 50°C. It should be noted that the purity of the synthesized undoped samples from these precursors made it possible to obtain samples in which the concentration of iron (fundamentally important in the context of our work), determined by the ICP was approximately 0.03 at.%. The content of cobalt and nickel impurities is an order of magnitude lower. The chemical compositions of the prepared samples are shown in Table 1. The acid treatment (HCl etching) was carried out for all the samples immediately after synthesis just as it was done in our work [20]. The analysis of the chemical composition of the samples was carried out by inductively coupled plasma (ICP) spectrometry.

The magnetic state was controlled by measuring the field dependence of magnetization at room temperature (RT) with the Faraday balance. The magnetic measurements in the temperature range of 2−350 K up to 70 kOe were performed using MPMS-XL (Quantum Design, USA). MathCad 14 and SciLab 6.0.2 software were applied to fit the magnetic measurements data. For the study of the magnetic properties before and after etching, four samples were used (S0, S1, S2, and S3) as given in Table 1.

The crystal structure and the phase composition of the as-prepared samples were checked by powder X-ray diffraction (XRD) using a Rigaku Dmax-2200 diffractometer with Cu Kα radiation ($\lambda = 1.54178$ Å). The broadening of X-ray diffraction patterns due to the microstructural and size effects was analysed by means of the Rietveld refinement using the TCH pseudo-Voigt peak profile function [22].

Ti L and Co L X-ray absorption spectra (XAS) were obtained at the Russian − German beamline at BESSY II (Berlin) in the surface-sensitivity total-electron yield (TEY) mode. The spectra were normalized to the beam current.

Electron paramagnetic resonance (EPR) measurements were performed on a Bruker ELEXSYS 580 pulse spectrometer in stationary mode. A powder sample was placed in a special quartz tube of 4 mm diameter. The spectra were registered at room temperature with a Super High-Q rectangular resonator. The interval of the constant magnetic field *B* was from 480 to 6000 Oe. The level of microwave power was 4.7 mW and the modulation amplitude was 1 Oe.

High-resolution transmission electron microscopy (TEM) on a JEM-2100 (JEOL) microscope was performed to determine the morphology of the synthesized nanopowders.

Table 1
Chemical compositions of the synthesized TiO_2:Co samples before and after etching with HCl as it was estimated by ICP mass spectrometry.

Samples	Co (at.%) before etching	Co (at.%) after etching	Fe (at.%)
S0	0.01	0.001	0.03
S1	0.33	0.30	0.03
S2	4.00	1.49	0.03
S3	8.44	5.81	0.03
S4	3.31	–	0.03
S5	1.70	–	0.03

3. Results

3.1. Electron microscopy

Fig. 1 shows a TEM image of the as-prepared undoped (S0, (a)) and Co-doped (S1, (b)) TiO_2 samples. It demonstrates that a disordered (or amorphous) TiO_2 lattice (denoted by symbol A) is detected on the surface of individual nanoparticles in the as-prepared state for both samples, S0 and S1. The origin of this disordered layer is unclear.

The TEM structures of samples S0 and S1 (Fig. 1 (a,b)) are similar. The size of nanoparticles was estimated to be about 20 nm (Fig. 1 (a)). The nanoparticles do not have a significant concentration of defects (Fig. 1 (b,c)). Fig. 1(d) shows a TiO_2 particle with a perfect boundary between twins.

3.2. XRD results

Fig. 2 presents X-ray diffraction patterns of samples S0, S3, and S4 in the as-prepared state. All the doped samples after synthesis are in the anatase phase, while XRD picture for the undoped sample

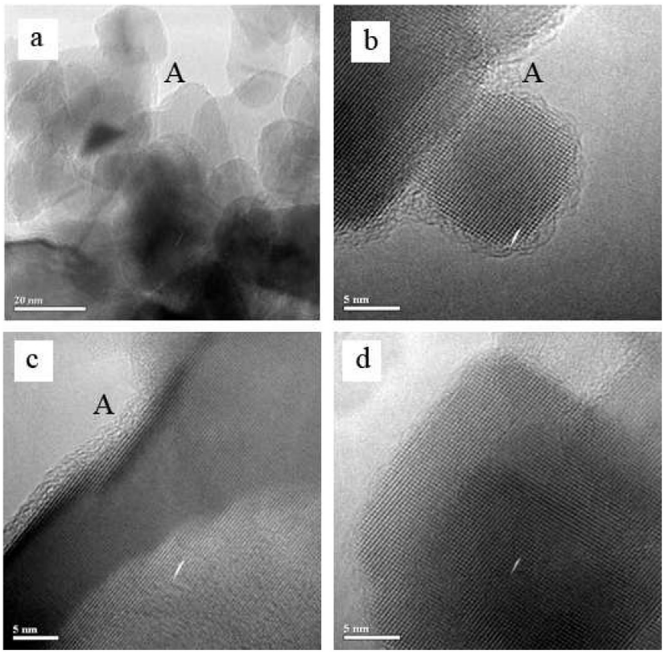

Fig. 1. (Colour online) (a) HRTEM pictures of undoped sample S0 and (b) doped S1 sample; (c) TEM picture of S1 sample at high magnification with the disordered regions denoted by A for all pictures (a,b,c). (d) The twinned particle of the sample S0.

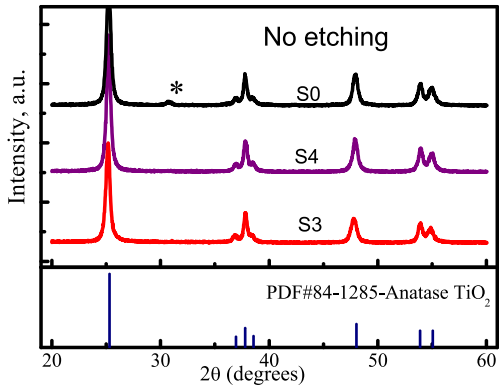

Fig. 2. (Colour online) X-ray diffraction patterns of the TiO_2:Co samples in the as-prepared state. The samples were not etched. The asterisk indicates a pattern of the brookite phase. (For interpretation of the references to color in this figure legend, the reader is referred to the Web version of this article.)

contents traces of the brookite phase (marked with an asterisk). The average effective coherent domain sizes estimated from the line width for all the samples are in the range of 15–20 nm which corresponds to the valued estimated from TEM experiments.

The absence of reflections from foreign phases on X-ray patterns does not exclude, for example, the formation of segregations containing cobalt and other impurities (e. g., iron), which are not recorded by X-ray analysis due to their high dispersion. In contrast to the X-ray diffraction studies, measurements of magnetic susceptibility allow to register a rather small content of magnetic impurities in the samples after etching.

3.3. Magnetic characterization

Magnetization curves $M(H)$ of all the samples before and after etching are presented in Fig. 3 (a, b). One can see that magnetization of the samples S1 (~ 0.3 at.%) and S2 (~1.5 at. %) after etching was decreased by 2–1.5 times in comparison with that of the samples in the initial state (Fig. 3 (a)). Relative changes of the magnetization of the samples before and after etching depend on the Co content. For the samples with low cobalt content, this change of the magnetization in the etched samples is less than that for the samples enriched by Co (e. g., sample S3).

Fig. 3 (b) shows the field dependencies of the magnetization at room temperature (RT) of sample S3 (about 8.4% of Co in the as-prepared state) before and after etching. A spontaneous magnetic moment of the as-prepared sample (S3, 8.4 at.% of Co) is observed (Fig. 3 (b)). Since magnetic cobalt oxides do not exist at RT, iron-containing segregations (about 0.03 at.% of Fe) can probably form a ferromagnetic contribution (FM) on the surface of as-prepared samples. In the process of the sol-gel synthesis, this contribution probably can be appeared due to the formation of magnetite or maghemite (or mixed oxides such as iron-cobalt ferrite). In the case of the appearance of Fe_3O_4 or γ-Fe_2O_3. the specific magnetization should be equal ~ 0.02 emu/g. It corresponds to the Fe content of ~ 0.03 at.% which is defined for all the samples (see Table 1). These data illustrate a very common experimental fact that the appearance of the ferromagnetism is determined only by magnetic contributions, which are formed mainly on the surface of the TiO_2 nanoparticles with 3*d* impurities.

In etched sample S3, the ferromagnetic contribution completely disappears (see Fig. 3 (b)). The paramagnetic contribution for sample S3 is decreased approximately by 1.6 times as a result of etching of paramagnetic Co^{2+}-ions as well. After etching of the samples some content of cobalt (Co^{2+}) and iron (Fe^{3+}) remains as a

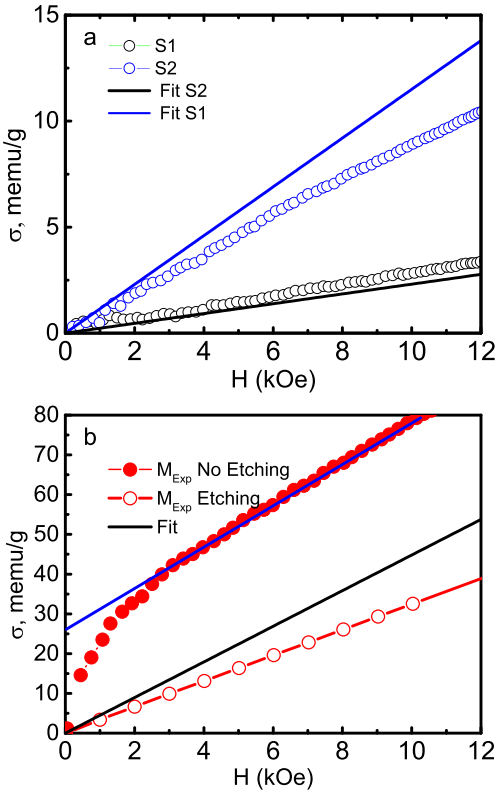

Fig. 3. (Colour online) Specific magnetization at RT for samples S1 and S2 after etching (a) and for sample S3 before and after etching (b). For comparison, for each sample, calculated sample of the magnetization (Brillouin function with $S = 3/2$) is given for non-interacting Co^{2+} ions in accordance with their actual concentrations in the samples. (For interpretation of the references to color in this figure legend, the reader is referred to the Web version of this article.)

solid solution in the TiO_2 lattice. The paramagnetic contribution of a solid solution of Co^{2+} in the samples is calculated, assuming that the magnetization is determined by non-interacting cobalt ions only. It can be seen that the magnetization of the paramagnetic contribution of cobalt ions with $S = 3/2$ at room temperature significantly exceeds the experimental value for all the samples (S2 and S3) with the exception of the sample with the low cobalt concentration. For sample S1 (0.3 at.% of Co), the magnetization is satisfactorily described mainly by a paramagnetic contribution in accordance with the Brillouin function. So, even at RT, we should propose the existence of the AFM contribution to explain the magnetization decrease.

3.4. EPR results

Electron paramagnetic resonance (EPR) spectroscopy is an effective probe for detection and characterization of paramagnetic centers and of a short-range magnetic order. It is known that the detection of a EPR signal from paramagnetic cobalt at RT, unfortunately, fails. However, these data can provide a very important information about some paramagnetic ions and defects (vacancies and radical oxygen) in Co-doped samples.

Fig. 4 shows normalized EPR spectra of the samples in the scale range of 300 Oe. The EPR spectrum contains a relatively wide central line, which presumably can be attributed to both oxygen vacancies and to, for example, radical oxygen and Fe^{3+} impurities [23]. The difference of *g* factors of this line for the undoped (g = 1.997) and Co-doped samples (g = 2.001) are observed, but the nature of that is not clear. For the undoped sample (S0), signals

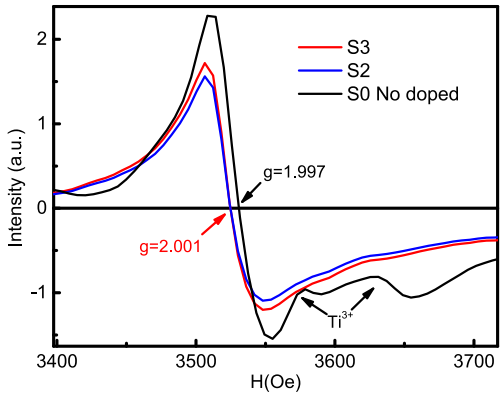

Fig. 4. (Colour online) Normalized EPR spectra of samples S0, S2 (1.49 at.% of Co), and S3 (5.81% of Co) with the field scan of 300 Oe. (For interpretation of the references to color in this figure legend, the reader is referred to the Web version of this article.)

from Ti^{3+} can be also observed. Note, the intensity of the central peaks with g factor of 1.997 (sample S0) and $g = 2.001$ (doped samples S2 and S3) remains almost unchanged with an increase in the cobalt content in the TiO_2 lattice by almost 4 times from 1.49 at.% of Co (sample S2) up to 5.81 at.% of Co (S3) (Fig. 4). The width of the central peak is about 40 Oe, which is significantly larger than that for a vacancy: the line width of F^+ vacancy according to Ref. [24] does not exceed 5–6 Oe. In our opinion, the width and the intensity of the central peak are determined mainly by the presence of Fe^{3+} ions. The traces from Fe^{3+} are also visible in the field region of approximately 1600 Oe with $g \simeq 4.3$ corresponding to rombohedral distorsion near Fe^{3+} [23] (not shown). The intensity of the central peak for undoped sample S0 is the same as for the samples doped with cobalt (Fig. 4). Hence, we should conclude that the all features of the EPR spectra can be explained by the existence only of the Fe^{3+} impurities in the samples. A reasonable explanation of the absence of changes in the width and the intensity of the central peak for all samples with different cobalt contents is that the Co^{2+} ions forming a solution prefer to occupy interstitial positions in the TiO_2 lattice rather than substitutional sites. Probably, in the case of TiO_2 doped with Co^{2+} ions, the formation of a substitutional solution should require too high energy to create vacancies. The location of Co ions in the interstitial sites does not require the creation the oxygen vacancies to provide the charge balance.

3.5. X-ray absorption spectroscopy

To understand the nature of magnetism in Co-doped TiO_2 nanopowders, it is very important to know oxidation states of Co-cations and its oxygen coordination environment. With this aim, we used soft X-ray absorption spectra. Ti L X-ray absorption spectra (XAS) of Co-doped (S5) and undoped (S0) TiO_2 nanopowders measured in total-electron yield mode are shown in Fig. 5. These spectra correspond to the Ti $2p \rightarrow$Ti $3d$ transition and are determined by the valence state of metal atoms. Spectral features labelled A – E are related to the Ti L_3 lines. The Ti L_2 lines consist of features F and G. The Ti L_3 and L_2 lines are split in the crystal field in t_{2g} (features A, B, C, and F) and e_g (features D, E, and G). The distance between t_{2g} and e_g related peaks in Ti $L_{2,3}$ XAS spectra does not exactly equal the crystal field splitting $10Dq$ since these spectra are strongly affected by correlation effects [25]. The pre-edge features A and B are due to $2p - 3d$ multiplet interactions [26].

The degree of oxidation of cobalt impurity ions in TiO_2:Co nanopowder can be estimated from Co L X-ray absorption spectra.

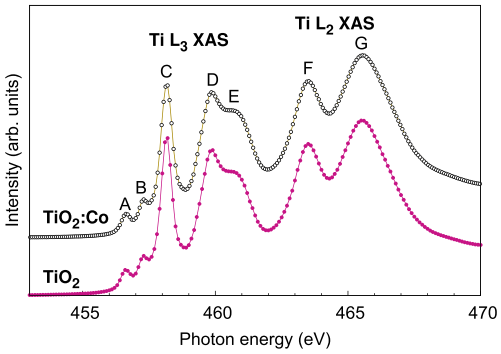

Fig. 5. (Colour online) Ti $L_{2;3}$ X-ray absorption spectra of TiO_2:Co (S5) and TiO_2 (S0) nanopowders. . (For interpretation of the references to color in this figure legend, the reader is referred to the Web version of this article.)

Fig. 6 shows a Co L_3 spectrum of TiO_2:Co. For interpretation of this spectrum, we used the CTM4XAS computer program taking into account the Coulomb and exchange interactions between $2p$ holes and $3d$ electrons, the splitting by the crystal field, spin – orbit interaction, and charge-transfer effects [27]. The results of calculations are shown in Fig. 6 also. In the calculations, the crystal field parameters $10Dq$ for the octahedral and tetrahedral environments were taken equal to 0.8 eV and −0.6 eV, respectively. The experimental spectrum is in good agreement with the calculation performed for Co^{2+} ions in a tetrahedral environment. Note, the Co^{2+} ions in a tretrahedral environment are in a high-spin spin state $S = 3/2$ only.

Summarizing the soft XAS results, one can conclude that both Ti^{4+} and Co^{2+} ions in TiO_2:Co nanopowders are tetrahedral coordinated by oxygen ions. Tetrahedrally coordinated Co^{2+} ions can be located in the both sites, interstitial and substitutional. Further, using density-functional theory calculations, we intend to show which tetrahedrally coordinated cobalt (interstitial or substitutional) is energetically favourable in the anatase lattice.

3.6. Theoretical calculations of exchange interactions within Co-pairs on DFT-based model

Density-functional theory (DFT) calculations were performed using the SIESTA pseudopotential code [28] as had been used successfully for related studies of impurities in bulk and thin-film morphologies of TiO_2 [29]. The calculations were made employing the Perdew – Burke – Ernzerhof variant of the generalized

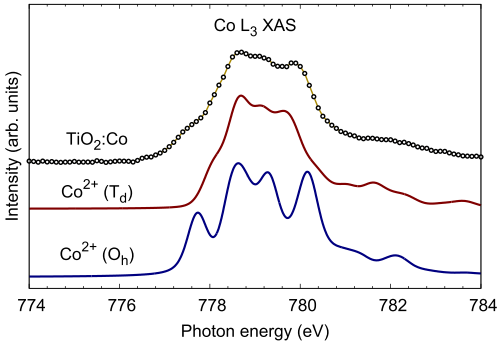

Fig. 6. (Colour online) Co L_3 X-ray absorption spectra of the TiO_2 and TiO_2:Co nanopowders (sample S5). Charge-transfer multiplet calculations for Co^{2+} ions in the oxygen octahedral (O_h) and tetrahedral (T_d) environments are shown. (For interpretation of the references to color in this figure legend, the reader is referred to the Web version of this article.)

gradient approximation (GGA – PBE) [30] for the exchange-correlation potential. After that, the calculated atomic positions were completely optimized. The ground electronic state was consistently found during optimization using norm-conserving pseudopotentials [31] for the cores, and a double-ξ plus polarization basis of localized orbitals for Co, Ti, and O. The forces and the total energies were optimized with an accuracy of 0.04 eV/Å and 1.0 meV, respectively for all discussed systems. All calculations were carried out with an energy mesh cut-off of 300 Ry and a *k*-point mesh of 6 × 6 × 4 in the Monkhorst – Pack scheme [32]. For our calculations, we used TiO_2 supercell of 96 atoms (see 6a,b,c). In our model, we consider a different combination of the Co ions such as substitutional (S) and interstitials (I) in the absence or in the presence of oxygen vacancies (v_O). The calculations of the formation energies (E_{form}) were based on the following formula:

$$E_{form} = [E_{total} - (E_{matrix} - mE_{Ti} + nE_{Co})] \Big/ m, \quad (1)$$

where E_{total} is the total energy of TiO_2, m is the number of cobalt impurities added in the supercell, and n is the number of Ti atoms removed from the supercell, E_{matrix} is the total energy of pure supercell, and E_{Co} and E_{Ti} are the total energies per atom of bulk Co and α-Ti, respectively. The value of exchange interactions are obtained within the Heisenberg model [17]:

$$E_{FM} - E_{AFM} = -2S_1S_2J, \quad (2)$$

where E_{FM} and E_{AFM} are the total energies of the same system with parallel and antiparallel orientations of spins on cobalt impurities and S_i is the value of the spins. Because the range of the exchange interactions in this system is rather long (Fig. 7 (b)), a spin of one atom in a supercell is also connected via exchange interaction with another Co-centre in a next supercell. For taking into account this effect, we introduce a factor two in formula (2). Note that in this approach, we calculate not an exact exchange between two Co-centers but an effective exchange for this configuration.

At the first step of our modelling, we examine which configuration of Co atoms is predominant in the studied samples. Results of the calculations (Fig. 8 (a) demonstrate that formation of the substitutional (S) 3*d* dopants is very energetically unfavourable. Probably due to the fact that when a divalent Co^{2+} ion is introduced into the lattice, an interstitial solution rather than substitutional one is preferably formed.

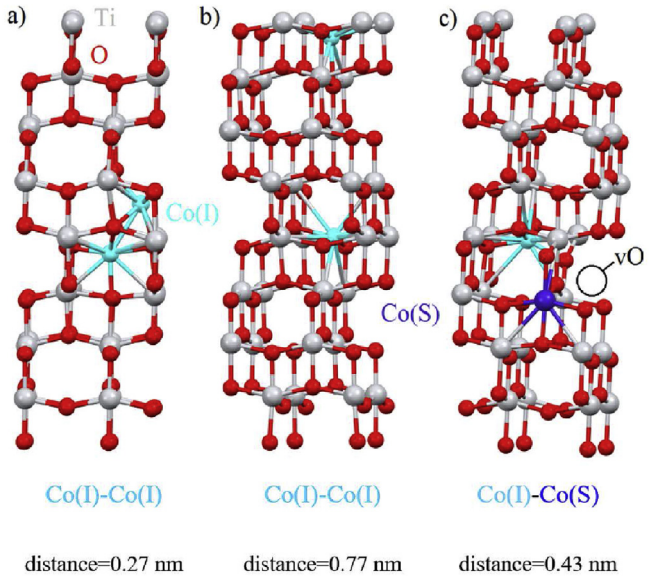

Fig. 7. (Colour online) (a, b) Optimized atomic structure of TiO_2 supercell with interstitial atoms (I) at different distances, (c) substitutional (S) and cobalt interstitial atoms (I) in vicinity of the oxygen vacancy (v_O). (For interpretation of the references to color in this figure legend, the reader is referred to the Web version of this article.)

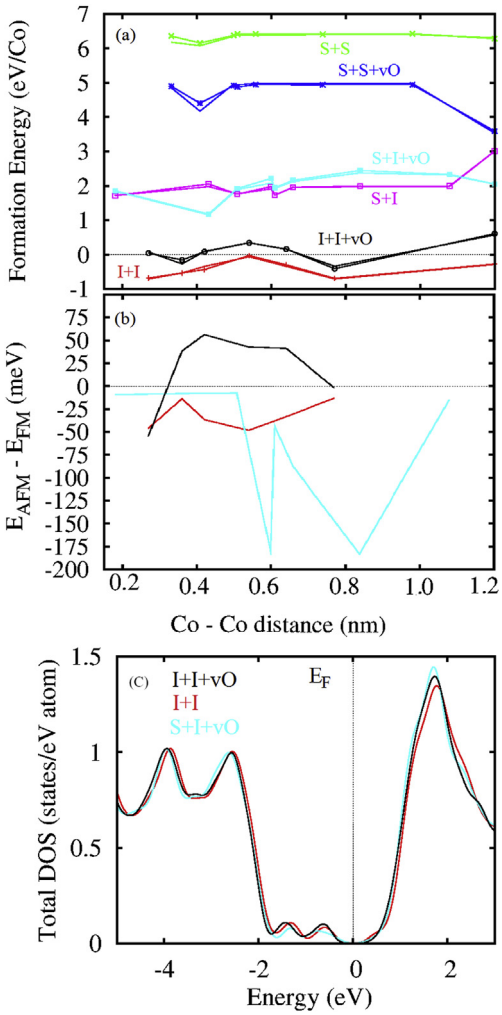

Fig. 8. (Colour online) (a) Calculated formation energies for various types of Co configurations as function of the distance between Co atoms. Results for non-collinear calculations are shown by lines with symbols. The values at the distance 1.2 nm are corresponding to single Co ions. (b) Calculated difference between antiferromagnetic and ferromagnetic orientations of Co-spins as function of distance for the three most probable types of Co defects configurations. The colors on panel (b) are corresponding to the colors on panel (a). (c) The total densities of states of the supercell with the most energetically favourable pair of Co-impurities from the probable types of configurations (I + I + v_O; I + I; S + I + v_O). (For interpretation of the references to color in this figure legend, the reader is referred to the Web version of this article.)

The presence of the oxygen vacancy decreases formation energies but it remains quite high. Note that in contrast to substitutional iron dopants in TiO_2 [20], cobalt ions do not demonstrate any tendency to the formation of pairs at the substitutional sites.

The most energetically favourable are interstitial positions (I + I). This type of Co-ions dimer (I + I) demonstrates a tendency of the formation of pairs with Co – Co antiferromagnetic exchange interactions of a value from −10 to −10 meV (Fig. 8 (a, b)). The presence of oxygen vacancies in vicinity of one of Co-impurities makes formation of these pairs less energetically favourable and turn exchange to ferromagnetic. Note that one of the energetically favourable I + I + v_o pairs corresponds to robust FM interactions. Thus, in the studied system, both types of magnetic interactions

(AFM and FM) present. Another type of defects that can be realized in the studied system is the combination of substitutional and interstitial defects at distance 0.43 nm in vicinity of an oxygen vacancy nearby substitutional impurity. Formation of other types of defects requires energies above 1.2 eV that makes formation of these configurations unprobable. Because cobalt has significant spin-orbital interactions, we also performed the calculation of the formation energies in non-collinear mode. Results of the calculations evidence the negligible contribution from spin-orbit coupling in the energetics of Co-ion formation (Fig. 8,(a)). This means that the reason for the decrease in magnetization compared to the magnetization of isolated Co^{2+} ions ($S = 3/2$) cannot be related to the influence of Co^{2+} anisotropy, which can complicate the magnetization process in high fields. To check possible non-collinearity of magnetic moments on Co-impurities on the surface, we have performed the calculations of the pair of substitutional and interstitial impurities on the (001) TiO_2 surface. Results of the calculations evidence that magnetic moments on both types of Co-defects are collinear even on the surface.

Thus, based on the results of the calculations, we can conclude that at the lowest concentrations, two different types of Co-pairs of interstitial sites (Fig. 7 (a) and 8 (a)) will prevail. Further increasing of the Co content should provide formation of the pairs for substitutional and interstitial Co atoms in vicinity of the oxygen vacancy (Fig. 7 (c), 8 (a)).

In contrast to the TiO_2:Fe where exchange interactions change steeply with increasing of the distance [20] in this system and especially in the case of configurations with interstitial Co atoms, magnetic interactions are varying unpredictable and remain non-negligible at long distances (Fig. 8 (b)). The cause of this difference is the appearance of Co-defect states in vicinity of Fermi level (Fig. 8 (c)) that makes magnetic properties extremely sensitive to the changes of electronic structure. Note that the larger magnitude of varying of the exchange interactions is observed for $S + I + v_O$ configuration (see Fig. 8 (b)) which has the states closest to Fermi level. It follows from the analysis of the calculation of the electronic structure that the TiO_2:Co system with cobalt is a semiconductor for he three representative highly probable configurations of defects (Fig. 8 (c)). Note that despite difference in type of defects and the absence or the presence of vacancies, the electronic structure of defect states remain almost the same. Thus, we can conclude that coordination and oxidation states of Co-impurities play decisive role in the electronic structure of defect states.

For determination of relations between theory and experiment, we performed the calculations of exchange integrals in the dimers. The data are summarized in Table 2.

As can be seen from Table 2 and Fig. 8 (a), the most energetically favourable configurations for the formation of dimers are the (I + I) configurations where interstitial atoms are situated at distances of approximately 0.27 nm and 0.77 nm. It also turns out that tetrahedral positions can be the most advantageous positions in these sites that is confirmed by XAS studies. Thus, the resulting interstitial solution based on TiO_2 leads to dimerization, but with a large set of energetically favourable dimers. Presumably, a larger amount of dimers types may be required to describe magnetic properties compared with the TiO_2:Fe system. Moreover, for favourable configurations ($I + I + v_O$) for TiO_2: Co, both positive and negative exchange interactions can be observed in dimers. However, the concentration of this configuration is limited from above by the content of vacancies in TiO_2 and may be only a few percent or even less. Therefore, the fraction of dimers with a positive exchange interaction is very small, but it cannot be completely excluded. It should be underlined that there is no necessity to attract the vacancy to form different negative exchange interactions inside the dimers.

Table 2
Calculated formation energies (E_{form}), magnetic moments (M) of Co ions, exchange integrals (J), and distances D between Co atoms for different configurations.

Configuration	E_{form} (eV)	D_{Co-Co} (nm)	M (μ_B)	J (K)
I + I	− 0.710	0.77	2.857	− 33
I + I	− 0.709	0.27	2.851	− 71
I + I	− 0.536	0.36	2.891	− 34
$I + I + v_O$	− 0.339	0.54	2.879	− 13
$I + I + v_O$	− 0.270	0.36	2.999	+96
$S + I + v_O$	+1.159	0.43	3.345 (S), 2.886 (I)	− 15

So, it should be emphasised that cobalt atoms, presumably, like iron atoms [20], are not distributed randomly over the TiO_2 lattice, but prefer to form dimers in interstitial sites. The value of the negative exchange interaction in the dimers is quite close, including dimers with the positive exchange interaction. At the same time, the results of experimental and theoretical studies completely exclude a ferromagnetic contribution in the refined TiO_2:Co samples.

It was found in a previous work on the analysis of the magnetic properties of the TiO_2: Fe system, that some part of iron atoms occupying titanium ions in octahedral positions form dimers in the TiO_2 matrix [20]. We are recognised that the model we used based on a mixture of single Fe ions and two types of dimers with different negative exchange interactions is probably a simplification and iron ions form not dimers, but more complex complexes (clusters), remaining at the sites of the anatase lattice. However, we still have no opportunity to carry out calculations for the cluster model, and we will try to use the same dimer model to describe magnetic properties of TiO_2:Co. As we can see below, an analysis of magnetic properties of the TiO_2:Co system in the frame of the dimer model gives a satisfactorily description of the experimental data.

4. Results of magnetic studies and discussion

4.1. Magnetic results

Field dependencies of the magnetization for samples S0, S1, S2, and S3 measured at low temperatures are shown in Fig. 9 (a, b). According to the chemical analysis, sample S0 contains about 0.03 at.% Fe, while the fraction of cobalt is less than 0.001%. Hence, the magnetism of sample S0 will be determined by the iron content only. Fig. 9 (a) shows the magnetization curve for sample S0 and the temperature dependence of the magnetic moment per iron atom with the mentioned concentration. The experimental value of the magnetic moment is approximately $4\mu_B$, which didnot much differ from the expected value of $5\mu_B$ for an Fe^{3+} ion presented by the Brillouin function (blue line) in Fig. 9 (a). A decrease of the magnetic moment of the iron ion may be due to the existence of $Fe^{3+} - Fe^{3+}$ dimers, as it was shown in Ref. [20] which can be formed in the TiO_2:Fe system even at low iron content. Thus, sample S0 contains probably a mixture of non-interacting iron ions and dimers with a negative exchange interaction with an approximate ratio of non-interacting Fe^{3+} magnetic carriers to the number of dimers as 80 : 20. Even in sample S0, the influence of dimers remains high enough.

Since iron is present in the samples S1, S2, and S3 doped with cobalt (about 0.03 at.% Fe), a correction of the magnetization was fulfilled for the all samples taking into account the mentioned iron content. Obviously, this correction of the magnetization (about 20%) is significant for sample S1 with a low cobalt content (0.3 at.%) while for the other samples (S2, S3) this correction does not exceed 5%.

In Fig. 9 (b), the magnetization of the TiO_2:Co samples is

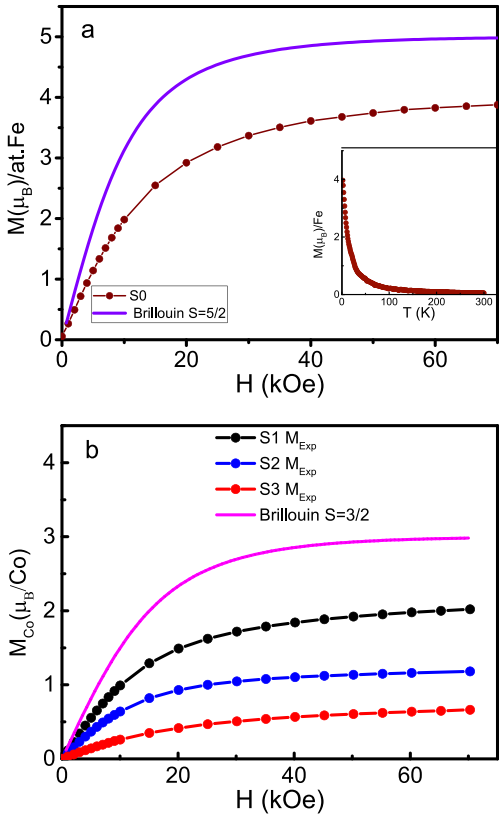

Fig. 9. (Colour online) (a) Experimental magnetization curve $M(\mu_B$ /Fe) of sample S0 at $T = 2$ K (dark red circles) and the calculated Brillouin function for high spin state the Fe^{3+} ions with $S = 5/2$ (violet solid line). In inset, the temperature dependence of the magnetization $M(\mu_B$ /Fe) of the S0 sample, $H = 50$ kOe is shown. (b) The experimental magnetization curves $M(\mu_B$ /Co) vs field at 2 K for samples S1, S2, and S3 and the calculated Brillouin function for the high-spin Co^{2+} ions ($S = 3/2$, $3\mu_B$/ Co). (For interpretation of the references to color in this figure legend, the reader is referred to the Web version of this article.)

represented in the Bohr magnetons per cobalt atom $M(\mu_B)$/ Co, which allows us to directly estimate a deviation of the experimentally measured magnetic moment from the calculated value given by the Brillouin function for isolated high-spin Co^{2+} ions with magnetic moment of $3\mu_B$. It seems, that the experimental value significantly less than the expected magnitude of the magnetic moment equal to $3\mu_B$, which corresponds to the Co moment in the high-spin state. The deviation of the experimental value of magnetic moments from value $3\mu_B$ significantly depends on the composition. For sample S3, these values is differed by 5 times (see Fig. 9).

This deviation cannot be explained by the presence of low-spin cobalt ions, since a low-spin state for Co^{3+} ions is impossible for tetrahedral coordination, which is established by the X-ray absorption spectra and by the DFT calculations. The most likely reason for the relatively low magnetization, similar to the TiO_2:Fe system [20], is the possible existence of cobalt dimers in TiO_2:Co compounds. So, we can assume that dimers with the negative exchange interactions can make a significant contribution to the magnetization process.

4.2. Dimer model

It turns out that the description of the magnetic properties of this system will be satisfactory when considering in the first rough approximation two types of dimers only in accordance to the previous paper [20]. As we suppose that two types of dimers are distinguished by values of exchange integrals J_1 and J_2, for simplicity $|J_2| > |J_1|$ [20]. The total moment per one $3d$ ion is described by the equation

$$M_{\text{total}}(B,T) = \frac{1}{N}\left[g\mu_B n_s B_s(B,T) + n_{d1}M(J_1,B,T) + n_{d_2}M(J_2,B,T)\right], \quad (3)$$

where B_s is the Brillouin function, n_{d1} and n_{d2} are the content of dimers with different exchange, respectively. The parameters of the spin model using the two types of dimers ($Co^{2+} - Co^{2+}$) and a paramagnetic contribution of Co^{2+} ions, which are required to describe with reasonable accuracy the magnetic properties of all samples (magnetization curves at different temperatures, at 2 and 300 K) and the temperature dependence of the magnetization at the field of 10 kOe are presented in Table 3.

Fig. 10 (a, b) shows the experimental magnetization curves of samples S1, S2, and S3 measured at 2 K and 300 K and the calculated curves in the model of thr two pairs and the paramagnetic contribution. As can be seen, a rather rough approximation by mainly two dimers satisfactorily describes the magnetization curves of all samples.

Fig. 11(a and b) shows the dependence $M(T)$ in the field of 10 kOe and the inverse relationship $1/M_{\text{Co}}(T)$ for samples S3 and S2, which is also satisfactorily described in the proposed model with the same two pairs and paramagnetic contribution (see Table 3). There is a good agreement between the Curie – Weiss constant θ which is determined from the experiment for sample S3 (in a field of 50 kOe) and from dimer model: $\theta = -40$ K and $\theta = -39$ K, respectively (Fig. 11 (b) anf Table 3). A reasonable agreement between the calculation of θ in the dimer model ($\theta = -19$ K) and the experiment ($\theta = -19$ K) is also observed for sample S2 (Fig. 11 (b); Table 3).

Although all exchange-coupled pairs at high temperature should be decay, correlations between the spins in the pairs are preserved. So the paramagnetic susceptibility of the system can be the sum of the susceptibility of individual Co ions and the susceptibilities of dimers of all types. The susceptibility of the dimer at high temperatures is described by a simple equation

$$\chi_d(J,T)|_{T\to\infty} = \frac{2C}{T - \Theta(J,s)}, \quad (4)$$

$$\Theta(J,s) = \frac{Js(s+1)}{3k_B}, \quad (5)$$

where J is the exchange interaction in the dimer, s is the spin value of Co, and Θ is the Weiss constant. This means that in the region of very high temperatures ($k_T \gg |J_{\max}|$), susceptibility is described by the sum of the Curie law and the Curie – Weiss laws. Therefore, $\chi^{-1}(T)$ should be a smooth function close to a straight line that slowly bends with decreasing temperature (see Fig. 11(a and b)).

Table 3
The model parameters to describe the experimental magnetization curves measured for S1, S2, S3 samples at low temperature (2 K) and room temperature (300 K). The following fitting parameters were used: content of dimers (n_{d1}) with small exchange interaction J_1, content of dimers (n_{d2}) with high exchange interaction J_2, total content of singles n_s, and coefficient of determination R_2 for $M(H)$ fitting at 2 K.

Samples	J_1 (K)	J_2 (K)	n_{d1} (%)	n_{d2} (%)	n_s (%)	R^2
S1	12 ± 2	–	49.2 ± 0.2	–	51 ± 0.2	0.9985
S2	15 ± 2	200 ± 20	49.2 ± 0.5	14.7 ± 0.2	36 ± 0.5	0.9865
S2	15 ± 1	200 ± 20	42.1 ± 0.6	37.8 ± 0.4	20 ± 0.2	0.9865

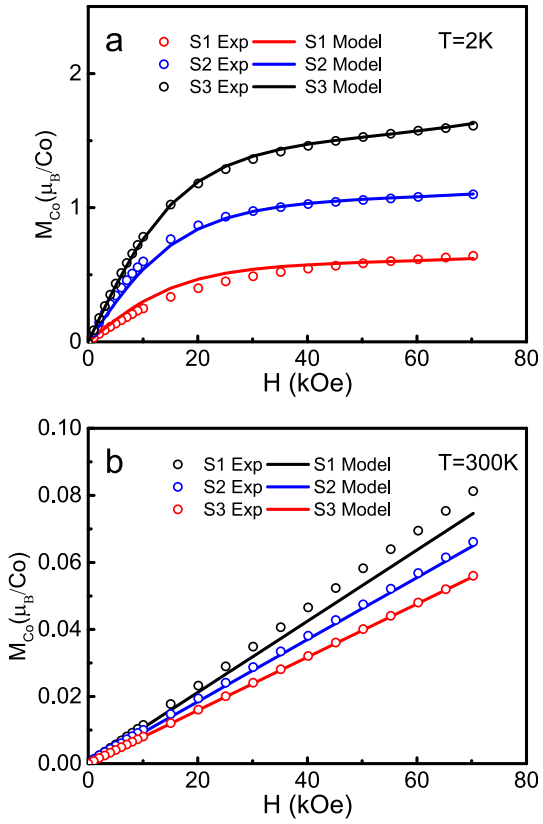

Fig. 10. (Colour online) Experimental curves (dots) and calculated magnetization curves (solid lines) of samples S1, S2, and S3 at 2 K (a) and 300 K (b) in the two-dimers model. The parameters of dimers and the value of paramagnetic contribution are given in Table 3. (For interpretation of the references to color in this figure legend, the reader is referred to the Web version of this article.)

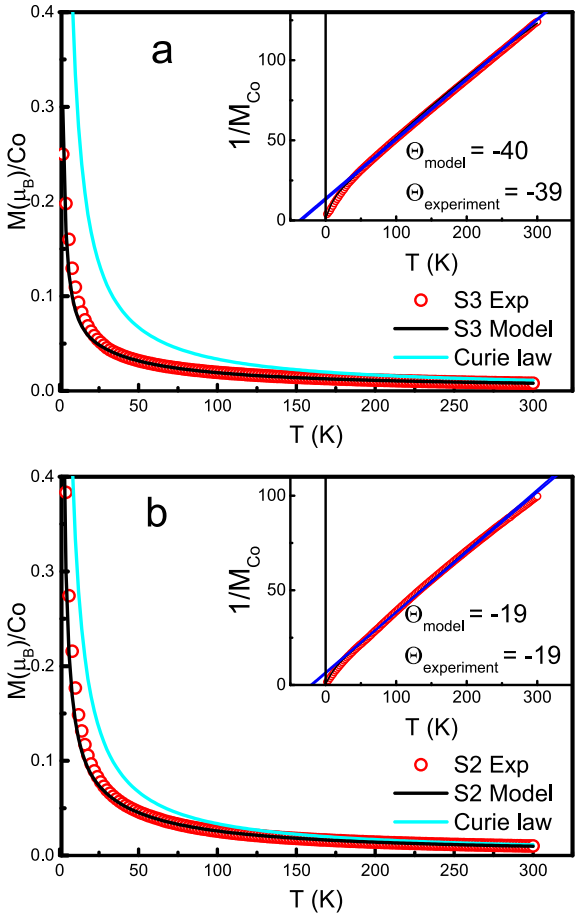

Figure 11. (Colour online) The temperature dependence of magnetic moment of Co atom at magnetic field of 10 kOe (experiment and model description (two pairs and singles) marked by black and red lines, respectively) are shown for sample S3 (a) and S2 (b). Cyan line is the Brillouin function for spin $S = 3/2$ for both samples. The reciprocal of $1/M_{Co}(T)$ for samples S3 and S2 are presented on the insets. The parameters of dimers and the paramagnetic contribution are given in Table 3.

This deviation of $\chi^{-1}(T)$ from the straight line is due to the fact that as T decreases, the average values of the dimer spins with large $|J|$ at $J<0$ gradually decrease so that their contributions to the system magnetization change. Therefore, the experimentally obtained value of the Weiss constant determines a certain average value of the exchange interaction parameter in a system with dimers with different exchange values. The average exchange in dimers was estimated to be $J \simeq -30$ K for $s = 3/2$ from equation (3). This experimental value, taking into account the averaging, is close to the theoretical estimates given in Table 2.

As expected, the content of paramagnetic Co^{2+} ions increases as the cobalt concentration decreases and reaches almost 51% for sample S1 (Table 3). So, even for this sample with small content of Co (sample S1) the magnetic behavior can be more or less satisfactorily described by the paramagnetic contribution and a rather high fraction of dimers (about 49%) with only one exchange parameter J of the order of -12 K (Table 3).

As can be seen from the data presented in Table 3, the content of dimers and the value of exchange interactions in dimers which are required to describe the samples depend on the Co content in TiO_2. So, an analysis of the properties in a very rough approximation (only two types of dimers plus isolated paramagnetic Co ions) gives a satisfactorily quantitative description of the magnetic properties of the TiO_2:Co.

5. Conclusions

In summary, we applied complementary methods for the studies of the refined Co-doped TiO_2 nanopowders synthesized by the hydrothermal method. It was established that the Co^{2+} ions have the high-spin state and located in the tetrahedral surrounding. It was shown by DFT calculations, that Co^{2+} ions prefer to occupy the interstitial positions in the TiO_2 lattice which are the most energetically favourable in compare to the substitutional sites. A substitutional replacement of Ti^{4+} for Co^{2+} requires high energy to create vacancies needed for the charge balance. It was shown by the EPR studies that there are no signals from vacancies (e. g., F^+ centers) at Co doping.

Thus, the TiO_2:Co system may be presented by non-interacting paramagnetic centers (Co^{2+} ions) and by a combination of various types of Co dimers, which are located, mainly, in the interstitial sites. The appearance of small amounts of dimers with positive coupling in the $(I + I + v_O)$ configuration was found on the base DFT calculations The ratio of the paramagnetic Co^{2+} ions and dimers content estimated from the magnetization curves at low temperature using the proposed model is strongly depend on the Co content in the samples. In any case the contribution of the dimers is a substantial part of the system even for the sample with relatively small Co content in the TiO_2 matrix. It was demonstrated that the quantum-mechanical model suggesting the paramagnetic Co^{2+} contribution and only two types of dimers $Co^{2+} - Co^{2+}$ with the different exchange interaction satisfactorily describes both the magnetization curves and the temperature dependence of

magnetization for all samples.

In the future, some experimental efforts should be undertaken to obtain direct experimental evidence of the existence of magnetic dimers (or clusters) in the TiO_2 matrix doped with 3*d* metals.

CRediT authorship contribution statement

Anatoly Ye Yermakov: Conceptualization. **Danil W. Boukhvalov:** Investigation. **Alexey S. Volegov:** Investigation. **Mikhail A. Uimin:** Investigation. **Galina S. Zakharova:** Investigation. **Alexander V. Korolev:** Formal analysis, Investigation. **Eugene V. Rosenfeld:** Investigation. **Vitaly V. Mesilov:** Investigation. **Artem S. Minin:** Methodology. **Vadim R. Galakhov:** Writing - original draft, Writing - review & editing. **Leonid S. Molochnikov:** Investigation. **Andrei F. Gubkin:** Investigation. **Aidar M. Murzakaev:** Investigation. **Sergey F. Konev:** Investigation.

Acknowledgement

The authors are grateful for the contributions made by our colleagues Prof. M. I. Kurkin, Drs. A. S. Konev, K. I. Borodin, and Z. A. Phattakhova. The authors are grateful to D. A. Smirnov for assistance in measurements on the BESSY-II synchrotron radiation source. The XRD and magnetic measurements have been performed in the Collaborative Access Centre of M. N. Mikheev Institute of Metal Physics of the Ural Branch of the Russian Academy of Sciences, Yekaterinburg, Russia. The XAS measurements were carried out according to the bilateral program "Russian – German Laboratory at BESSY". The research was supported by the Russian Foundation of Basic Research (Grant 17-02-00093) and partly by the state assignment of Ministry of Science and Higher Education of the Russian Federation (theme "Magnet", No AAAA-A18-118020290129-5 and theme "Electron", No AAAA-A18-118020190098-5.

References

[1] L.M.C. Pereira, J.P. Araújo, V. Bael, Experimentally evaluating the origin of dilute magnetism in nanomaterials related content practical limits for detection of ferromagnetism, J. Phys. D Appl. Phys. 50 (2017) 393002, https://doi.org/10.1088/1361-6463/aa801f.

[2] J.M. Coey, M. Venkatesan, P. Stamenov, Surface magnetism of strontium titanate, J. Phys. Condens. Matter 28 (2016) 1–38, https://doi.org/10.1088/0953-8984/28/48/485001.

[3] M. Murakami, Y. Matsumoto, T. Hasegawa, P. Ahmet, K. Nakajima, T. Chikyow, H. Ofuchi, I. Nakai, H. Koinuma, Cobalt valence states and origins of ferromagnetism in Co doped TiO^2 rutile thin films, J. Appl. Phys. 95 (2004) 5330–5333, https://doi.org/10.1063/1.1695598.

[4] A.M. Mudarra Navarro, C.E. Rodríguez Torres, V. Bilovol, A. Fabiana Cabrera, L.A. Errico, M. Weissmann, Study of the relation between oxygen vacancies and ferromagnetism in Fe-doped TiO^2 nano-powders, J. Appl. Phys. 115 (2014) 223908, https://doi.org/10.1063/1.4883183.

[5] J.D. Bryan, S.A. Santangelo, S.C. Keveren, D.R. Gamelin, Activation of high-$^{T}_{c}$ ferromagnetism in Co^{2+}:TiO^2 and Cr^{3+}:TiO^2 nanorods and nanocrystals by grain boundary defects, J. Am. Chem. Soc. 127 (2005) 15568–15574, https://doi.org/10.1021/ja0543447.

[6] K.A. Griffin, A.B. Pakhomov, C.M. Wang, S.M. Heald, K.M. Krishnan, Intrinsic ferromagnetism in insulating cobalt doped anatase TiO^2, Phys. Rev. Lett. 94 (2005) 157204, https://doi.org/10.1103/PhysRevLett.94.157204.

[7] B. Santara, P.K. Giri, K. Imakita, M. Fujii, Evidence of oxygen vacancy induced room temperature ferromagnetism in solvothermally synthesized undoped TiO^2 nanoribbons, Nanoscale 5 (2013) 5476–5488, https://doi.org/10.1039/c3nr00799e.

[8] C.E. Stoner, Collective electron ferronmagnetism, Proc. Royal Soc. Lond. Ser. A. Mathem. Phys. Sci. 165 (1938) 372–414, https://doi.org/10.1098/rspa.1938.0066.

[9] Y.F. Zhao, C. Li, S. Lu, L.J. Yan, Y.Y. Gong, L.Y. Niu, X.J. Liu, Effects of oxygen vacancy on ^{3d}transition-metal doped anatase TiO:^{2} First principles calculations, Chem. Phys. Lett. 647 (2016) 36–41, https://doi.org/10.1016/j.cplett.2016.01.040.

[10] J. Osorio-Guillén, S. Lany, S.V. Barabash, A. Zunger, Nonstoichiometry as a source of magnetism in otherwise nonmagnetic oxides: magnetically interacting cation vacancies and their percolation, Phys. Rev. B 75 (2007) 1–9, https://doi.org/10.1103/PhysRevB.75.184421.

[11] A.S. Semisalova, Y.O. Mikhailovsky, A. Smekhova, A.F. Orlov, N.S. Perov, E.A. Gan'shina, A. Lashkul, E. Lähderanta, K. Potzger, O. Yildirim, B. Aronzon, A.B. Granovsky, Above room temperature ferromagnetism in Co- and V-doped TiO^2 —- revealing the different contributions of defects and impurities, J. Supercond. Nov. Magnetism 28 (2015) 805–811, https://doi.org/10.1007/s10948-014-2776-9.

[12] L.A. Errico, M. Rentería, M. Weissmann, Theoretical study of magnetism in transition-metal-doped TiO^2 and $TiO^{2-\delta}$, Phys. Rev. B 72 (2005) 1–8, https://doi.org/10.1103/PhysRevB.72.184425.

[13] A. Vasiliev, O. Volkova, E. Zvereva, M. Isobe, Y. Ueda, S. Yoshii, H. Nojiri, V. Mazurenko, M. Valentyuk, V. Anisimov, I. Solovyev, R. Klingeler, B. Büchner, Barium vanadium silicate $BaVSi^2O^7$: a $^{t}_{2g}$counterpart of the Han purple compound, Phys. Rev. B 87 (2013) 1–8, https://doi.org/10.1103/PhysRevB.87.134412.

[14] A. Twardowski, H.J. Swagten, W.J. De Jonge, M. Demianiuk, Magnetic behavior of the diluted magnetic semiconductor $Zn^{1-x}Mn_xSe$, Phys. Rev. B 36 (1987) 7013–7023, https://doi.org/10.1103/PhysRevB.36.7013.

[15] H. Alawadhi, I. Miotkowski, A. Lewicki, A.K. Ramdas, S. Miotkowska, M. McElfresh, Magnetic susceptibility and compositional dependence of the energy gap in $Cd^{1-x}Co_xTe$, J. Phys. Condens. Matter 14 (2002) 4611–4620, https://doi.org/10.1088/0953-8984/14/17/330.

[16] T.E. De Souza, A. Mesquita, A.O. De Zevallos, F. Béron, K.R. Pirota, P.P. Neves, A.C. Doriguetto, H.B. De Carvalho, Structural and magnetic properties of dilute magnetic oxide based on nanostructured Co-doped anatase TiO^2 ($Ti^{1-x}Co_xO^{2-\delta}$), J. Phys. Chem. C 117 (2013) 13252–13260, https://doi.org/10.1021/jp4017129.

[17] W. Heisenberg, On the theory of ferromagnetism, Z. Phys. 61 (1930) 206–219, https://doi.org/10.1007/BF01339661.

[18] G. Temple, P.A.M. Dirac, The principles of quantum mechanics, Math. Gaz. 19 (1935) 301, https://doi.org/10.2307/3606137.

[19] J.H.V. Vleck, The Theory of Electric and Magnetic Susceptibilities, vol. 18, Oxford University Press, Oxford, 1934, https://doi.org/10.2307/3605487.

[20] A.Y. Yermakov, A.F. Gubkin, A.V. Korolev, L.S. Molochnikov, M.A. Uimin, E.V. Rosenfeld, M.I. Kurkin, A.S. Minin, A.S. Volegov, D.W. Boukhvalov, S.F. Konev, Formation of Fe–Fe antiferromagnetic dimers in doped TiO^2:Fe nanoparticles, J. Phys. Chem. C 123 (2019) 1494–1505, https://doi.org/10.1021/acs.jpcc.8b10553.

[21] A.Y. Yermakov, G.S. Zakharova, M.A. Uimin, M.V. Kuznetsov, L.S. Molochnikov, S.F. Konev, A.S. Konev, A.S. Minin, V.V. Mesilov, V.R. Galakhov, A.S. Volegov, A.V. Korolyov, A.F. Gubkin, A.M. Murzakayev, A.D. Svyazhin, K.V. Melanin, Surface magnetism of cobalt-doped anatase TiO^2 nanopowders, J. Phys. Chem. C 120 (2016) 28857–28866, https://doi.org/10.1021/acs.jpcc.6b10417.

[22] P. Thompson, D.E. Cox, J.B. Hasting, Rietveld refinement of Deybe-Scherrer synchrotron X-ray data from Al2O3, Jorunal of Apply Crystallographica 20 (1987) 79–83.

[23] F. Tolea, M.N. Grecu, V. Kuncser, S.G. Constantinescu, D. Ghica, On the role of Fe ions on magnetic properties of doped TiO^2 nanoparticles, Appl. Phys. Lett. 106 (2015) 142404, https://doi.org/10.1063/1.4917037.

[24] M. Chiesa, M. Paganini, S. Livraghi, E. Giamello, Charge trapping in TiO^2 polymorphs as seen by electron paramagnetic resonance spectroscopy, Phys. Chem. Chem. Phys. 15 (2013) 9435–9447, https://doi.org/10.1039/c3cp50658d.

[25] F.M. De Groot, J.C. Fuggle, B.T. Thole, G.A. Sawatzky, L2,3 x-ray-absorption edges of d0 compounds: K+, Ca2+, Sc3+, and Ti4+ in Oh (octahedral) symmetry, Phys. Rev. B 41 (1990) 928–937, https://doi.org/10.1103/PhysRevB.41.928.

[26] J.P. Crocombette, F. Jollet, Ti ^{2p}x-ray absorption in titanium dioxides $(TiO)^2$: the influence of the cation site environment, J. Phys. Condens. Matter 6 (1994) 10811–10821, https://doi.org/10.1088/0953-8984/6/49/022.

[27] E. Stavitski, F.M.F. de Groot, The CTM4XAS program for EELS and XAS spectral shape analysis of transition metal L edges, Micron 41 (2010) 687–694, https://doi.org/10.1016/j.micron.2010.06.005.

[28] J.M. Soler, E. Artacho, J.D. Gale, A. García, J. Junquera, P. Ordejón, D. Sánchez-Portal, The SIESTA method for ab initio order-N materials simulation, J. Phys. Condens. Matter 14 (2002) 2745–2779, https://doi.org/10.1088/0953-8984/14/11/302, arXiv:0111138.

[29] B. Leedahl, D.A. Zatsepin, D.W. Boukhvalov, E.Z. Kurmaev, R.J. Green, I.S. Zhidkov, S.S. Kim, L. Cui, N.V. Gavrilov, S.O. Cholakh, A. Moewes, Study of the structural characteristics of ^{3d}metals Cr, Mn, Fe, Co, Ni, and Cu implanted in ZnO and TiO-^{2}experiment and theory, J. Phys. Chem. C 118 (2014) 28143–28151, https://doi.org/10.1021/jp509761c.

[30] J.P. Perdew, K. Burke, M. Ernzerhof, Generalized gradient approximation made simple, Phys. Rev. Lett. 77 (1996) 3865–3868, https://doi.org/10.1103/PhysRevLett.77.3865.

[31] N. Troullier, J.L. Martins, Efficient pseudopotentials for plane-wave calculations, Phys. Rev. B 43 (1991) 1993–2006, https://doi.org/10.1103/PhysRevB.43.1993.

[32] H.J. Monkhorst, J.D. Pack, Special points for Brillouin-zone integrations, Phys. Rev. B 13 (1976) 5188–5192, https://doi.org/10.1103/PhysRevB.13.5188.